J. Appl. Comput. Mech., 12(4) (2026) 1411-1426
DOI: 10.22055/jacm.2025.48708.5441

ISSN: 2383-4536
jacm.scu.ac.ir

Shahid Chamran University of Ahvaz

Journal of Applied and Computational Mechanics

Research Paper

# Longitudinal Control of Electric Vehicles under One-Pedal Driving Conditions Considering Tire–Road Friction Capacity

**Hadi Sazgar[1], Ali Keymasi-Khalaji[2]**

[1] Department of Mechanical Engineering, Iranian Research Organization for Science and Technology (IROST), Tehran, Iran, Email: sazgar@irost.ac.ir

[2] Department of Mechanical Engineering, Faculty of Engineering, Kharazmi University, Tehran, Iran, Email: keymasi@khu.ac.ir

Received August 22 2025; Revised November 26 2025; Accepted for publication November 27 2025.
✉ Corresponding author: A. Keymasi-Khalaji (keymasi@khu.ac.ir)
© 2025 Published by Shahid Chamran University of Ahvaz

**Abstract.** As electric vehicles become more widespread, precise motion control is increasingly vital. The present study introduces a robust and stable control algorithm designed for the longitudinal guidance of electric vehicles operating under "one-pedal driving" conditions. The algorithm explicitly accounts for tire saturation by setting controller gains based on maximum tire-road friction. It integrates speed and position controllers derived from Lyapunov theory, ensuring asymptotic stability. Obtained results across varied driving conditions confirm that the proposed controller maintains vehicle stability and achieves superior path-tracking accuracy compared to conventional feedback methods. Moreover, it produces smoother control torque, reducing powertrain wear and power consumption—key advantages for improving efficiency and durability in electric vehicles.

**Keywords:** Vehicle longitudinal dynamics, Speed control, Position control, Tire saturation limit, Robust control.

## 1. Introduction

### 1.1. Background

With increasing global emphasis on environmental sustainability and the rapid advancement of clean energy technologies, electric vehicles (EVs) have emerged as a viable and environmentally friendly alternative to traditional internal combustion engine (ICE) vehicles [1]. Unlike ICE vehicles, EVs employ distinct mechanical and control architectures, particularly in their powertrain and regenerative braking systems [2]. A notable innovation in EV operation is the “one-pedal driving” feature, which enables the driver to control both acceleration and deceleration using a single pedal [3]. This capability reduces reliance on mechanical brakes, leading to simplified vehicle design, lower maintenance costs, and improved energy recovery efficiency [4].

### 1.2. Formulation of the problem of interest

Despite its advantages, implementing precise and stable control for EVs operating in one-pedal driving mode presents several challenges. During aggressive maneuvers or low-adhesion conditions, tires can operate beyond their linear range and approach force saturation, resulting in highly nonlinear vehicle dynamics [5]. Under such circumstances, maintaining accurate speed and position tracking becomes difficult. Given that tires play a critical role in overall vehicle stability [6, 7], it is essential to design control algorithms that explicitly incorporate tire saturation effects into their formulation. This study addresses the problem of robust longitudinal motion control of EVs under these challenging conditions.

### 1.3. Literature survey

Numerous control strategies have been developed for longitudinal guidance of EVs and autonomous vehicles. Reference [8] provides a comprehensive review of speed control techniques for electric vehicles. Chu et al. [9] analyzed longitudinal motion control algorithms used in adaptive cruise control systems. Advanced single-pedal control strategies based on nonlinear model predictive control (NMPC) have been proposed to enhance energy efficiency and ride comfort [10]. Jalali et al. [11] introduced an integrated control and estimation framework combining traction control and speed estimation based on tire dynamics. For longitudinal position control, several methods have been reported. Reference [12] presented a Linear Quadratic Integral Tracking (LQIT) approach for robust path tracking, while [13] employed an extended state observer for disturbance rejection. Qin et al. [14] proposed a modified sliding mode controller effective in both acceleration and braking conditions. Hybrid methods combining fuzzy logic and sliding mode control have been proposed to improve robustness [15]. Deep reinforcement learning-based controllers have also been explored to optimize comfort and safety [16]. In [17], an adaptive cruise control algorithm for autonomous vehicles is developed using a sliding mode control approach, implemented with Arduino and ultrasonic sensors. Zhou et al. [18] proposed a model-based adaptive sliding mode speed control algorithm that relies solely on wheel speed sensors and is suitable for diverse

Published online: November 29 2025

driving environments. In [19], a model predictive control (MPC) approach is introduced for the longitudinal dynamics of electric vehicles, along with a mass estimation algorithm to adapt to varying loads. Wang et al. [20] proposed a hybrid control strategy for the speed control of unmanned vehicles, effective during both acceleration and deceleration modes. In [21], a combined feedback and feedforward control approach is applied for vehicle longitudinal acceleration control. Oudjama et al. [22] developed a robust H-infinity controller based on Linear Matrix Inequalities (LMI) theory for the speed control of electric vehicles. While these studies have contributed significantly to improving EV longitudinal control, most assume linear tire behavior or neglect the effects of tire force saturation. A review of the existing literature indicates that, although several studies have partially addressed the issue of tire force saturation [23-25], there remains a gap in developing control strategies that systematically and explicitly integrate tire saturation constraints into the design.

### 1.4. Scope and contribution of this study

To address the tire saturation limitations, this study proposes a robust and stable control algorithm for longitudinal speed and position tracking of electric vehicles under one-pedal driving conditions. The key innovation lies in explicitly incorporating tire saturation constraints into the control design. Controller gains are determined according to the maximum tire–road friction capacity, ensuring stability and smooth torque delivery even under nonlinear tire dynamics. Using Lyapunov-based methods, both speed and position controllers are formally proven to achieve asymptotic stability. Compared with conventional feedback controllers, the proposed algorithm improves path-tracking accuracy, reduces torque fluctuation, minimizes powertrain wear, and enhances energy efficiency during critical driving scenarios.

### 1.5. Organization of the paper

The remainder of this paper is structured as follows: Section 2 describes the dynamic model of the vehicle. Section 3 outlines the proposed control algorithm, encompassing both speed and position control modes. Section 4 reviews the results obtained for longitudinal speed and position control. Finally, Section 5 provides a conclusion and discusses potential directions for future research.

## 2. Dynamic Model

Various dynamic models of varying complexity have been documented in the literature for the longitudinal dynamics of vehicles [26]. The appropriate dynamic model for the intended application will be presented in Fig. 1.

This model includes three degrees of freedom ($v, \omega_f, \omega_r$), that $v$ represents the vehicle's longitudinal speed, $\omega_f$ denotes the angular velocity of the front axle wheels and $\omega_r$ represents the angular velocity of the rear axle wheels. The vehicle's longitudinal equation of motion can be expressed as follows:

$$m\dot{v} = F_{xf} + F_{xr} - mg\sin\theta - F_a \tag{1}$$

where $m$ is the mass of the vehicle, $F_{xf}$ is the total longitudinal force of the front axle tires, $F_{xr}$ is the total longitudinal force of the rear axle tires, $g$ is the gravitational acceleration, and $\theta$ represents the road slope. In Eq. (1), $F_a$ denotes the aerodynamic force, which can be calculated using the following equation:

$$F_a = \frac{1}{2}\rho C_d A_F \left(v + v_{\text{wind}}\right)^2 \tag{2}$$

where $\rho$ is the air density, $C_d$ is the aerodynamic drag coefficient, $A_F$ is the effective frontal area of the vehicle, and $v_{\text{wind}}$ represents the wind speed.

Given a front-axle propulsion configuration, this wheel dynamics can be stated as follows:

$$\begin{cases} J_w\dot{\omega}_f = T_f - r_w F_{xf} - r_w f_{\text{roll}} F_{zf}\cos\theta \\ J_w\dot{\omega}_r = -r_w F_{xr} - r_w f_{\text{roll}} F_{zr}\cos\theta \end{cases} \tag{3}$$

In the above equations, $J_w$ represents the rotational inertia of the wheel, $r_w$ refers to the effective wheel radius, $T_f$ represents the driving torque of the front axle, $f_{roll}$ denotes the rolling resistance coefficient of the tire, $F_{zf}$ is the vertical load on the front axle, and $F_{zr}$ is the vertical load on the rear axle as follows:

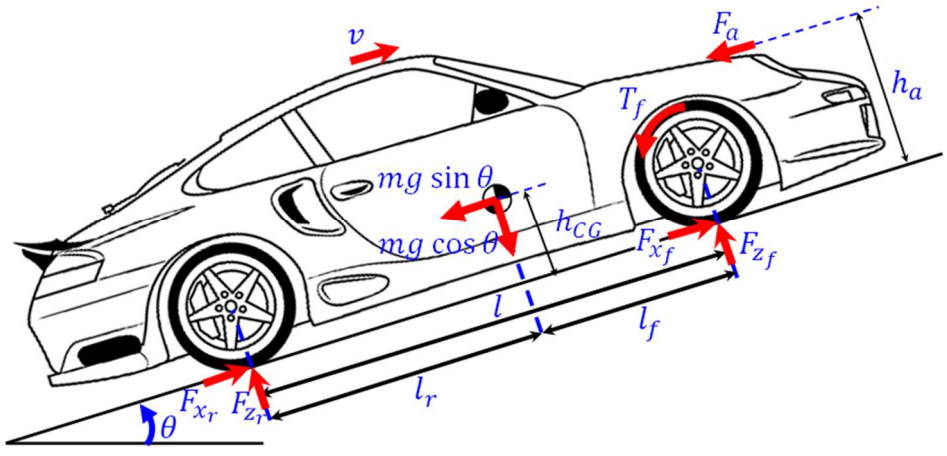


**Fig. 1.** Vehicle longitudinal dynamic block diagram.

$$F_{z_f} = \left[\frac{-mh_{CG}(\dot{v} + g\sin\theta) - F_a h_a + mgl_r\cos\theta}{l_f + l_r}\right] \tag{4}$$

$$F_{z_r} = \left[\frac{mh_{CG}(\dot{v} + g\sin\theta) + F_a h_a + mgl_f\cos\theta}{l_f + l_r}\right] \tag{5}$$

Based on the Pacejka Magic Formula, the longitudinal tire forces can be determined using the following expression [27]:

$$F_{x_\tau} = \mu_\tau F_{z_\tau}, \quad \tau \in \{f, r\} \tag{6}$$

$$\mu_\tau = D_\tau \sin[C_\tau \arctan(B_\tau \sigma_\tau)], \quad \tau \in \{f, r\} \tag{7}$$

$$\sigma_\tau = \frac{v_{rw_\tau} - v}{\max(v_{rw_\tau}, v)}, \quad \tau \in \{f, r\} \tag{8}$$

where $\mu$ is the coefficient of friction between the tire and the road, $\sigma$ is the longitudinal slip of the tire, and $B$, $C$, and $D$ are the tire model coefficients. Additionally, $v_{rw}$ is the velocity of the wheel's contact point with the road surface, which is calculated using Eq. (9):

$$v_{rw_\tau} = r_w\omega_\tau, \quad \tau \in \{f, r\} \tag{9}$$

To account for the dynamics of the gearbox, electric motor, inverter, drive, control unit, and other components, it is assumed that the relationship between the requested torque from the powertrain (reference torque: $T_{fr}(s)$) and the torque applied to the wheel hub ($T_f(s)$) is given by the following equation:

$$\frac{T_f(s)}{T_{fr}(s)} = \frac{\omega_n^2}{s^2 + 2\xi\omega_n + \omega_n^2} \tag{10}$$

where $\omega_n$ is the natural frequency and $\xi$ is the damping ratio.

The specifications of the vehicle dynamic system are presented in Table 1.

## 3. Control Algorithm Design

The proposed control algorithm is a type of feedback control that consists of two parts: vehicle speed control and position control. This algorithm is robust against disturbances and parameter variations, and it also considers the tire saturation limit when determining the control input. The control algorithm ensures that the longitudinal tire force, $F_x$, remains within the permissible limit, $F_{max}$. The control input employed is the torque applied to the front wheels, denoted as $T_f$. The procedure is as follows: First, the value of $F_{xf}$ is designed based on Eq. (1). Then, using the front wheel dynamics (Eq. (3)), the required reference torque ($T_{fr}$) calculated. This reference torque is then sent to the powertrain system, which applies the actual torque $T_f$ to the wheel hub.

It is worth noting that this study is conducted under a one-pedal driving mode. Therefore, the longitudinal force on the rear axle is negligible and is always less than $F_{max}$. The details of the control algorithm design will be presented in the following sections.

### 3.1. Speed control

Assuming that $v_r$ is the reference speed, the vehicle speed tracking error is defined as follows.

$$e = v - v_r \tag{11}$$

**Theorem 1.** Considering the control input in the form of Eq. (12)., and assuming $K > 0$, the speed tracking error dynamics given in Eq. (11) will be stable around the origin:

$$F_{xf} = -mK\tanh e - F_{xr} + F_a + mg\sin\theta + m\dot{v}_r \tag{12}$$

**Proof.** A Lyapunov candidate function can be written as:

$$V = \frac{1}{2}e^2 \tag{13}$$

**Table 1.** Vehicle specifications.

| Symbol | Value | Units | Symbol | Value | Units |
|---|---|---|---|---|---|
| $m$ | 1346 | kg | $r_w$ | 0.282 | m |
| $l_f$ | 1.56 | m | $J_w$ | 3.264 | kg.m$^2$ |
| $l_r$ | 1.04 | m | $f_r$ | 0.015 | --- |
| $h_{CG}$ | 0.5 | m | $B$ | 25 | --- |
| $h_a$ | 1.39 | m | $C$ | 1.5 | --- |
| $C_d$ | 0.335 | --- | $D$ | 0.5 | --- |
| $A_F$ | 2 | m$^2$ | $\rho$ | 1.225 | kg/m$^3$ |

By computing the derivative of the proposed Lyapunov function, we obtain:

$$\dot{V} = e\dot{e} = e(\dot{v} - \dot{v}_r) \tag{14}$$

By replacing $\dot{v}$ from Eq. (1) into Eq. (14), the following expression for $\dot{V}$ is derived as:

$$\dot{V} = e\left(\frac{1}{m}\left[F_{xf} + F_{xr} - mg\sin\theta - F_a\right] - \dot{v}_r\right) \tag{15}$$

By substituting the expression for $F_{xf}$ from Eq. (12) into Eq. (15), we obtain:

$$\dot{V} = -\frac{K}{m}e\tanh e \tag{16}$$

By choosing $K > 0$, the derivative of the Lyapunov candidate function becomes negative definite, and asymptotic stability is guaranteed.

- **Determination of the Permissible Range for the Control Gain (K)**

For simplification, it is assumed that $F = -F_{xr} + F_a + mg\sin\theta + m\dot{v}_r$. Therefore, Eq. (12) can be rewritten as:

$$F_{xf} = -mK\tanh e + F \tag{17}$$

From the vehicle dynamics perspective, to maintain stability, the tire force must not exceed the tire saturation limit. Assuming that the maximum friction coefficient is $\mu_{max}$, the tire saturation limit is given by $F_{max} = \mu_{max} F_{zf}$. Therefore, the following inequality can be derived from the tire saturation constraint:

$$\left|F_{xf}\right| \le F_{max} \tag{18}$$

By combining Eq. (17) and Eq. (18), we have:

$$\left|F - mK\tanh e\right| \le F_{max} \tag{19}$$

It should be noted that $F$ is a variable and depends on several factors, such as vehicle acceleration, vehicle speed, and road angle. Also, in general, the values of $F$ and $e$ can be positive, negative, or zero.

Therefore, the value of $K$ cannot be directly calculated from inequality (19). Considering that $|\tanh e \le 1|$, during the calculation of $K$, the value of $\tanh e$ is taken as its maximum value, which is one. To solve the problem, depending on the sign of the error, one of the following cases of inequality (19) will occur:

$$\begin{aligned} &|F| \le F_{max} && e = 0 \\ &|F - mK| \le F_{max} && e > 0 \\ &|F + mK| \le F_{max} && e < 0 \end{aligned} \tag{20}$$

**Case #1: $e = 0$**

In this case, based on Eq. (20)., it can be observed that the control signal does not rely on $K$ and is instead a function of $F$.

**Case #2: $e > 0$**

Inequality (20), can be rewritten in the following form:

$$-F_{max} \le F - mK \le F_{max} \qquad e > 0 \tag{21}$$

In addition to inequality (21), for the stability of the control loop, it is necessary that $K > 0$. Therefore, for $e > 0$, the following three inequalities must be satisfied concurrently to determine the value of $K$:

$$mK \le F + F_{max} \tag{22}$$

$$mK \ge F - F_{max} \tag{23}$$

$$mK > 0 \tag{24}$$

For better understanding, each of the inequalities is considered a line, and all three lines are plotted on the $mK$ - $F$ plane as shown in Fig. 2. The common region that satisfies all three conditions is shown in green. According to this figure, for $e > 0$, if $F > -F_{max}$, one can take $mK = F + F_{max}$. However, if $F \le -F_{max}$, the tire saturation criterion will be considered.

**Case #3: $e < 0$**

Similarly, in this case, inequality (20) can also be reformulated as follows:

$$-F_{max} \le F + mK \le F_{max} \qquad e > 0 \tag{25}$$

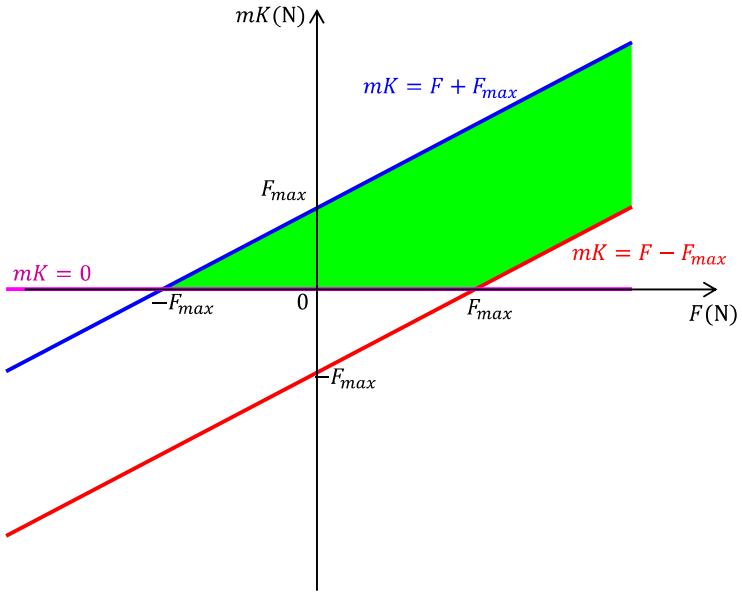


**Fig. 2.** The allowable region for controller gain (K) in $mK$ - $F$ diagram when $e > 0$.

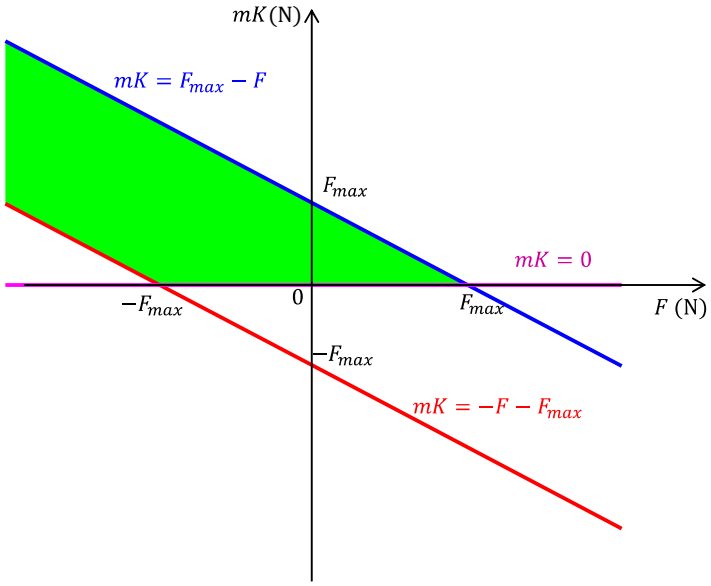


**Fig. 3.** The allowable region for controller gain (K) in $mK$ - $F$ diagram when $e < 0$.

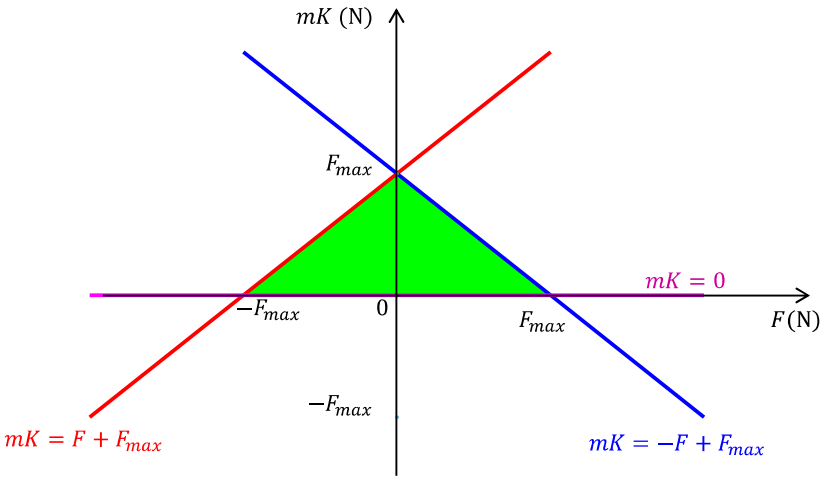


**Fig. 4.** The allowable region for controller gain (K) in $mK$ - $F$ diagram.

In addition to inequality (25), the control loop stability condition requires that $K > 0$ at all times. Therefore, under the condition $e < 0$, the following three inequalities must be considered to determine $K$:

$$mK \le F_{max} - F \tag{26}$$

$$mK \ge -F - F_{max} \tag{27}$$

$$mK > 0 \tag{28}$$

The three lines corresponding to the above inequalities are shown in Fig. 3. In Fig. 3, the common region that satisfies all three conditions is shown in green. According to this figure, for $e < 0$, if $F \le -F_{max}$, one can take $mK = F_{max} - F$. However, if $F > -F_{max}$, the tire saturation criterion will be considered.

By carefully comparing Fig. 2 and Fig. 3, it can be observed that regardless of the sign of the error, both figures share a common triangular region, which is shown in Fig. 4. Therefore, for closed-loop stability and to satisfy the tire saturation limit, it is sufficient to choose $mK$ within this triangular region. Based on Fig. 4, the maximum permissible value of $mK$ for all error cases is selected. Utilizing Eq. (17), the longitudinal tire force $F_{xf}$ can then be computed as:

$$F_{xf} = \begin{cases} F_{max}\text{sign}(F) & |F| > F_{max} \\ (-F + F_{max})\tanh e + F & F \ge 0 \\ (F_{max} + F)\tanh e + F & F < 0 \end{cases} \tag{29}$$

where sign denotes the sign function.

### 3.2. Position control

Assuming that $x_r$ is the reference position, the vehicle position tracking error and its derivative are defined as

$$\begin{aligned} e &= x - x_r \\ \dot{e} &= \dot{x} - \dot{x}_r \end{aligned} \tag{30}$$

where $\dot{x}$ and $\dot{x}_r$ represent the vehicle speed and the desired speed, respectively.

**Theorem 2.** Considering the control input in the form of Eq. (31), assuming $K_1, K_2 > 0$, the position tracking error dynamics given in Eq. (30) are stable around the origin:

$$F_{xf} = -mK_1 \tanh e - mK_1 \tanh \dot{e} - F_{xr} + F_a + mg\sin\theta + m\ddot{x}_r \tag{31}$$

**Proof.** By substituting $F_{xf}$ from Eq. (31) into Eq. (1), the following closed-loop system equation is obtained:

$$m(\ddot{x} - \ddot{x}_r) - mK_1 \tanh e - mK_2 \tanh \dot{e} = 0 \tag{32}$$

By further simplification, we have:

$$\ddot{e} - K_1 \tanh e - K_2 \tanh \dot{e} = 0 \tag{33}$$

Assuming $K_1 > 0$ and $K_2 > 0$, the error dynamic is stable, and therefore the position tracking error will converge to zero.

- **Determination of the permissible range for the control gains ($K_1$, $K_2$)**

For simplicity, it is assumed that $F = -F_{xr} + F_a + mg\sin\theta + m\ddot{x}_r$. Consequently, Eq. (31) can be reformulated into the form presented in Eq. (31):

$$F_{xf} = -mK_1 \tanh e - mK_2 \tanh \dot{e} + F \tag{34}$$

Similar to the speed control section, to maintain the stability of the vehicle dynamics, inequality (18) must always hold. By combining Eq. (18) and Eq. (34), we have:

$$|F - mK_1 \tanh e - mK_2 \tanh \dot{e}| \le F_{max} \tag{35}$$

If $e$ and $\dot{e}$ are zero, the conditions will be similar to the case of $e = 0$ in the speed control section. Also, if the error or its derivative is zero, the allowable ranges for $K_1$ and $K_2$ can be calculated using the method presented in the speed control section. The results are shown in Fig. 5.

In situations where both the error and its derivative are nonzero, we are essentially faced with a single equation involving two unknowns, $K_1$ and $K_2$, which prevents their direct determination, as was possible in the speed control section. To address this issue, the values of $\tanh e$ and $\tanh \dot{e}$ are assumed to be their maximum value, which is one. Additionally, it is assumed that the following relationship holds between $K_1$ and $K_2$:

$$K_1 = rK_2 \quad r > 1 \tag{36}$$

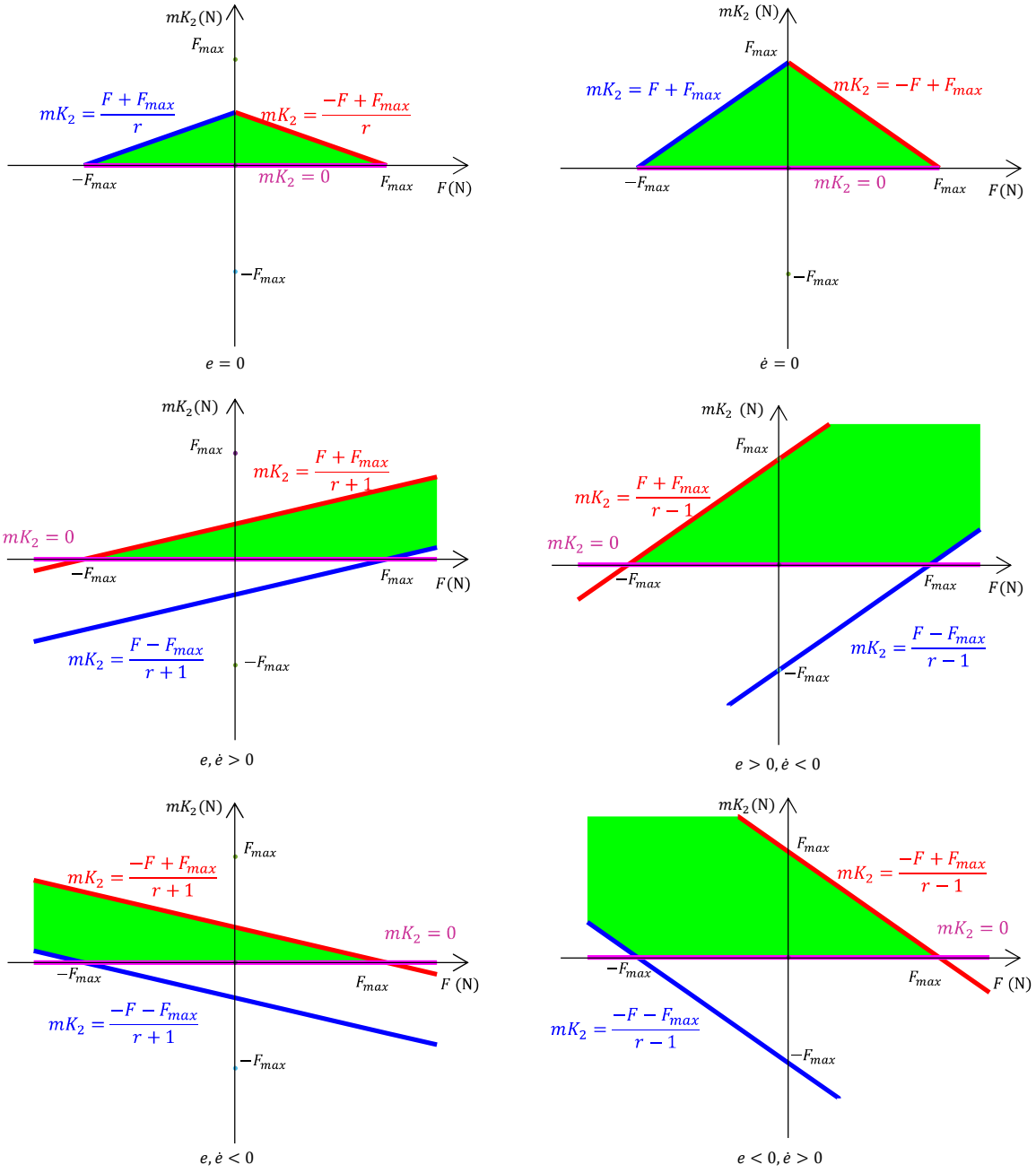


**Fig. 5.** The allowable region for controller gain ($K_2$) in the $mK_2$ - $F$ diagram for different cases of $e, \dot{e}$.

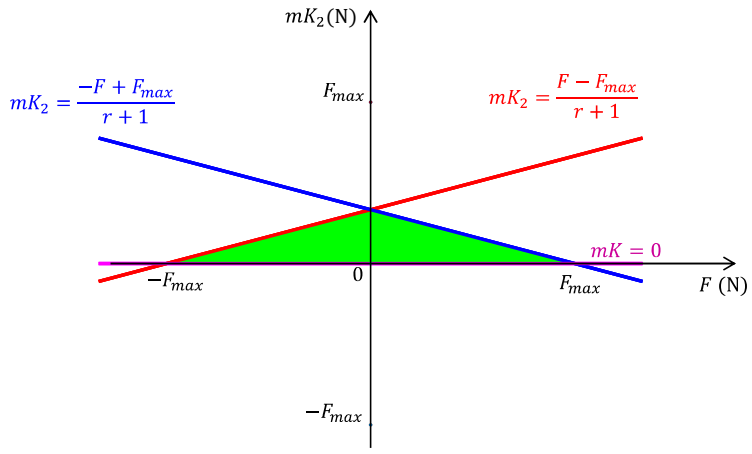


**Fig. 6.** The allowable region for controller gain ($K_2$) in the $mK_2$ - $F$.

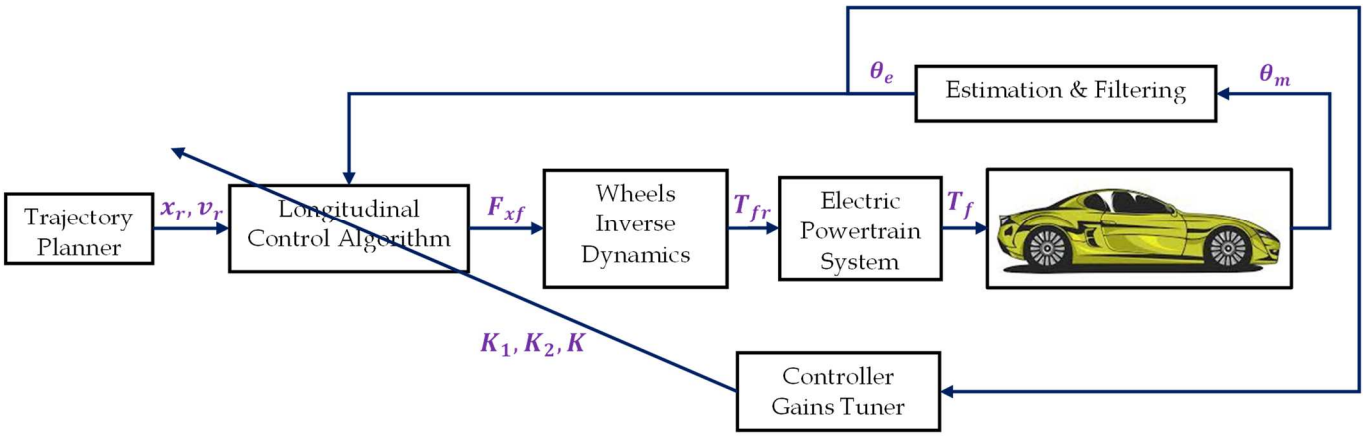


**Fig. 7.** Block diagram of the control algorithm.

Now, considering Eq. (36), for the remaining cases of error and error derivative, one of the following conditions will occur.

$$\begin{aligned} &|F - m(r+1)K_2| \le F_{\max} && e,\dot{e} > 0 \\ &|F - m(r-1)K_2| \le F_{\max} && e > 0, \dot{e} < 0 \\ &|F + m(r+1)K_2| \le F_{\max} && e,\dot{e} < 0 \\ &|F + m(r-1)K_2| \le F_{\max} && e < 0, \dot{e} > 0 \end{aligned} \tag{37}$$

Similar to the method described in the speed control section, the allowable region for $K_2$ can be determined based on the different signs of the error and its derivative. The results are shown in Fig. 5.

A detailed analysis of Fig. 5 reveals that irrespective of the sign of the error and its derivative, all cases share a common triangular region, as depicted in Fig. 6. Consequently, choosing $mK_2$ within this region is sufficient to guarantee closed-loop stability and compliance with tire saturation limits.

Based on Fig. 6, by choosing the maximum value of $mK_2$ applicable to all error and error derivative conditions, and utilizing Eq. (31) and Eq. (36), the longitudinal tire force $F_{xf}$ can be determined as

$$F_{xf} = \begin{cases} F_{\max}\,\mathrm{sign}(F) & |F| > F_{\max} \\ -\dfrac{r(F_{\max} - F)}{r+1}\tanh e - \dfrac{F_{\max} - F}{r+1}\tanh \dot{e} + F & F \ge 0 \\ -\dfrac{r(F_{\max} + F)}{1+r}\tanh e - \dfrac{F_{\max} + F}{r+1}\tanh \dot{e} + F & F < 0 \end{cases} \tag{38}$$

where sign denotes the sign function.

To facilitate a clearer understanding of the proposed control algorithm, its block diagram is illustrated in Fig. 7. The Trajectory Planner block is responsible for generating the reference trajectory. In the Longitudinal Control Algorithm, the required longitudinal force is computed based on the reference trajectory and the estimated current state of the vehicle. The tuning of the control algorithm gains is performed by the Controller Gains Tuner. The Wheels Inverse Dynamics block converts the calculated longitudinal force into the wheel torque. The Electric Powertrain System encompasses components such as the differential, electric motor, drive unit, inverter, motor control unit, and other related subsystems. Since certain variables, such as road friction, cannot be directly measured due to the absence of appropriate sensors, their values must be estimated. Additionally, sensor data are often contaminated with noise and therefore require filtering. Estimating unmeasured variables and filtering sensor data are carried out within the Estimation & Filtering block. In this block, $\theta_m$ denotes the vector of input variables, while $\theta_e$ represents the vector of output variables. The main focus of this study is on the Longitudinal Control Algorithm and the Controller Gains Tuner.

## 4. Obtained Results

In this section, the results of the proposed control algorithm are presented. To enable a more comprehensive evaluation of the proposed control strategy, all maneuvers have also been implemented using a conventional feedback controller that does not consider tire saturation effects. For the sake of brevity, the proposed control algorithm will be referred to as FCTS (Feedback Control with Tire Saturation), whereas the conventional feedback controller will be denoted as FC (Feedback Control) throughout this paper. In these implementations, the maximum torque applied to the front axle wheels is set to 2500 N.m during acceleration and 2000 N.m during regenerative braking. The maneuvers are performed on a low-friction road, where the maximum tire-road friction coefficient is assumed to be 0.5. In implementing the proposed controller, the usable friction coefficient is constrained to 90% of the tire's maximum capacity, corresponding to a value of 0.45.

The subsequent sections provide a detailed analysis of the controllers' performance and a comparative evaluation based on the results.

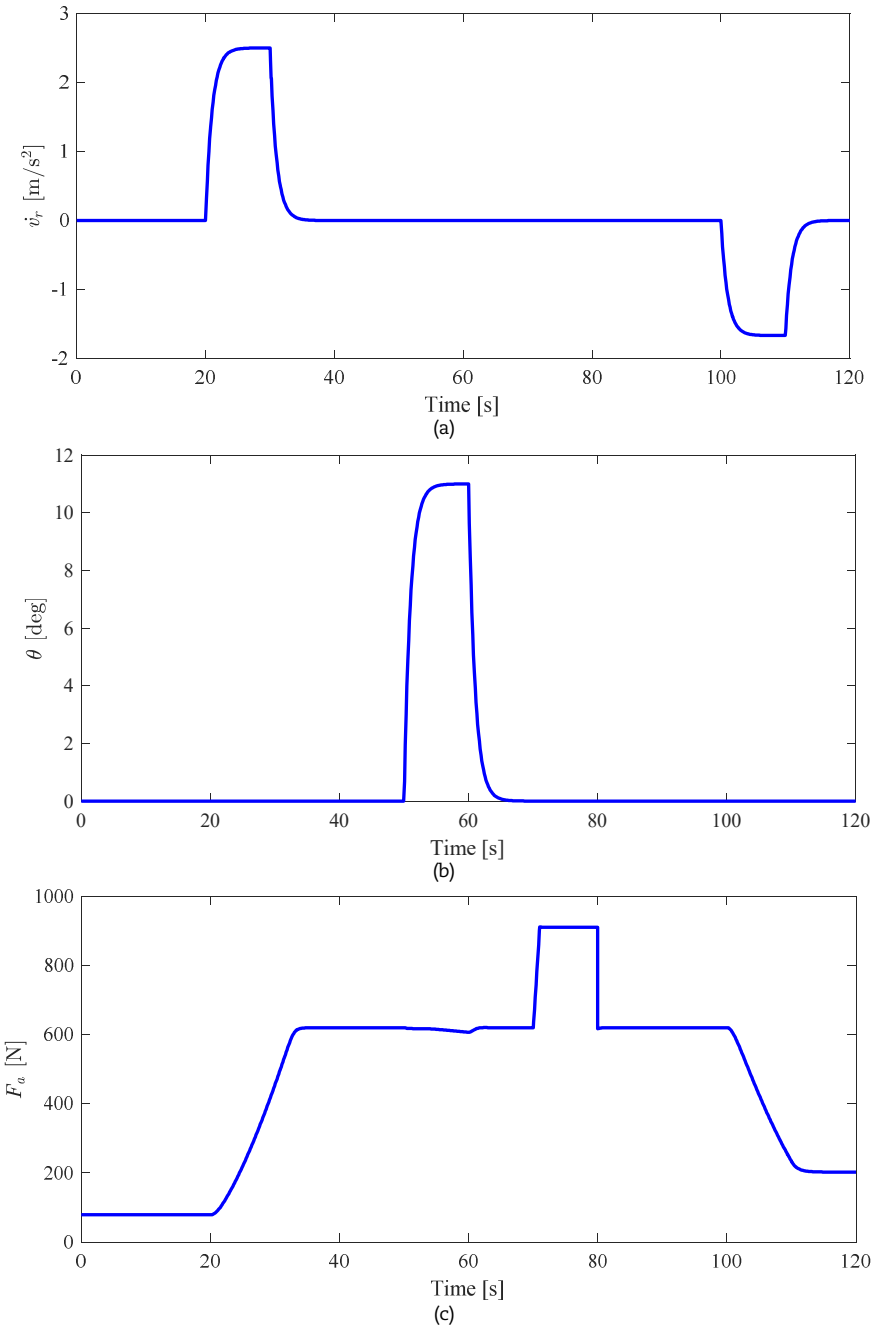


**Fig. 8.** Speed control: (a) Acceleration, (b) Road slope, (c) Aerodynamic force disturbance.

### 4.1. Longitudinal speed control

The specifications of the designed scenario for evaluating speed control are illustrated in Fig. 8. As observed in Fig. 8(a), the acceleration is set to 2.5 m/s$^2$ from 20 to 30 seconds and -1.5 m/s$^2$ from 100 to 110 seconds. The remainder of the maneuver is conducted at a constant speed. Furthermore, according to Fig. 8(b), the road slope is 11 deg between 50 and 60 seconds, while it remains zero for the rest of the maneuver. To account for disturbance effects, it is assumed that between 70 and 80 seconds, the longitudinal wind speed is 30 km/h. This disturbance causes a sudden 30% increase in aerodynamic force (Fig. 8(c)). The total duration of the maneuver is considered to be 120 seconds.

To evaluate the tracking error of the proposed controller, the velocity profiles and velocity tracking errors are presented in Fig. 9. Examination of Fig. 9(a) reveals that, in terms of reference speed tracking, the performance of the FCTS controller is significantly superior to that of the FC controller. A comparison of the error magnitudes is clearly illustrated in Fig. 9(b). According to this figure, the worst-case tracking error for the FCTS controller is approximately 11 km/h, whereas for the FC controller, it reaches about 27 km/h.

Regarding the robustness of the FCTS controller, it is observed that despite the application of disturbances (aerodynamic force) between 70 and 80 seconds, the controller was still able to manage the disturbance and accurately track the reference trajectory effectively. Analyzing the control input signals shown in Fig. 10. reveals interesting results. In the torque variation curves applied to the front wheels, it can be seen that for the FC controller, the torque reaches the upper allowable limits during both acceleration and regenerative braking modes. However, in the FCTS algorithm, the torque levels remain significantly lower. This aspect is vital from the energy consumption perspective in electric vehicles. Additionally, in the FC controller, a severe torque oscillation (from 2500 N.m to -2000 N.m) occurs around 35 seconds, which is highly undesirable regarding powertrain wear and the impact forces applied to the vehicle.

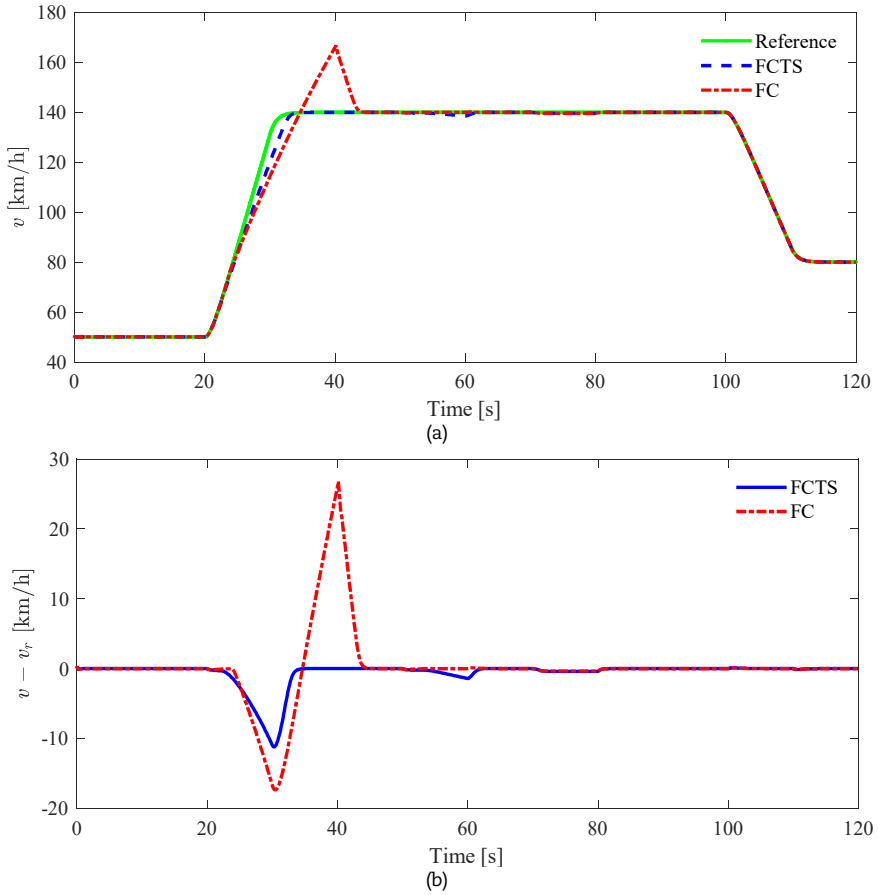


**Fig. 9.** Reference speed tracking, (a) Speed, (b) Speed tracking error.

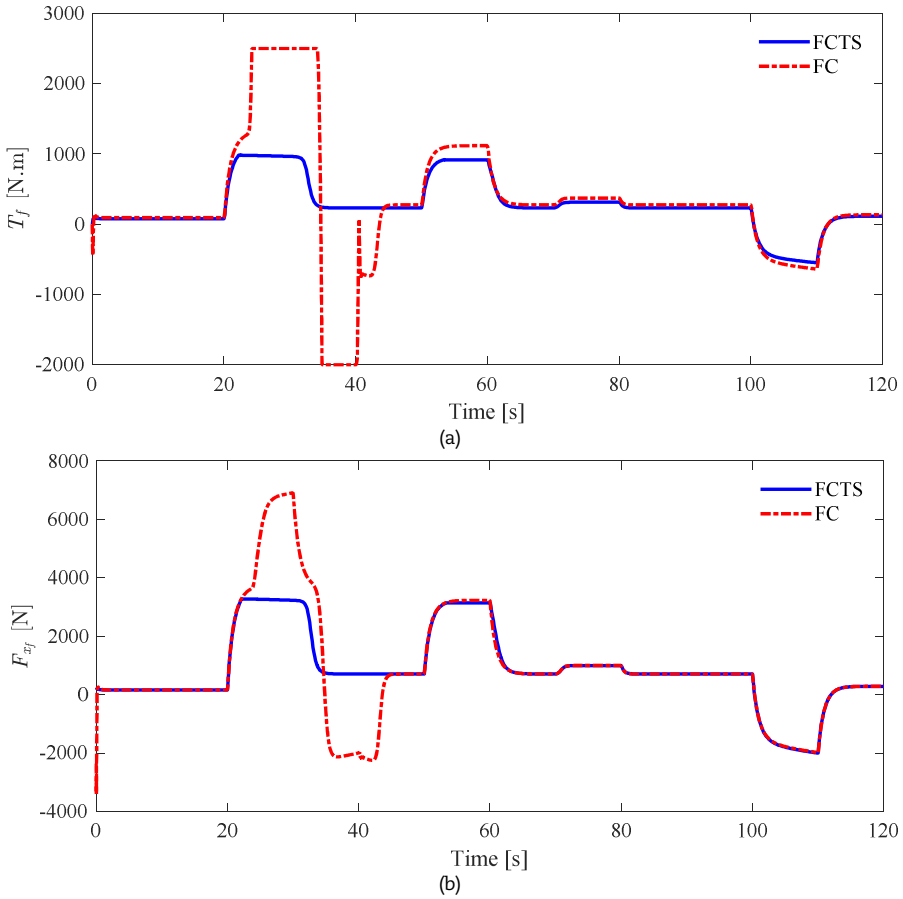


**Fig. 10.** Speed control inputs, (a) Torque, (b) Longitudinal tire force, (c) Tire-road friction coefficient.

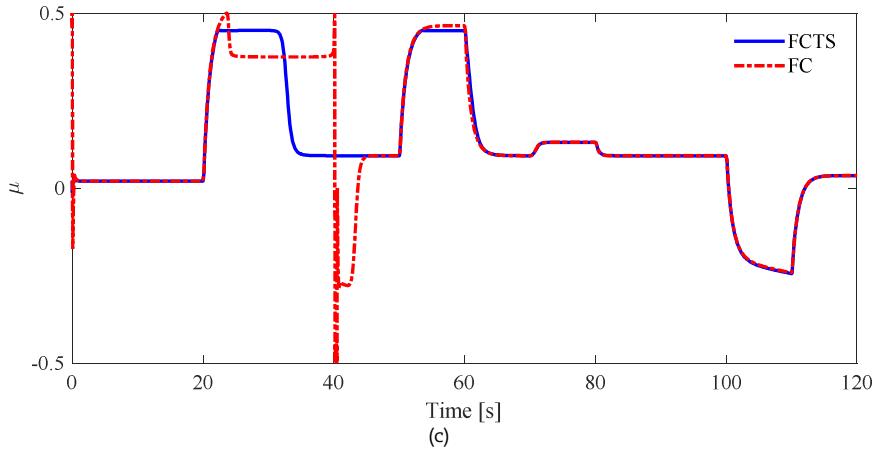


(c)

**Fig. 10.** Continued.

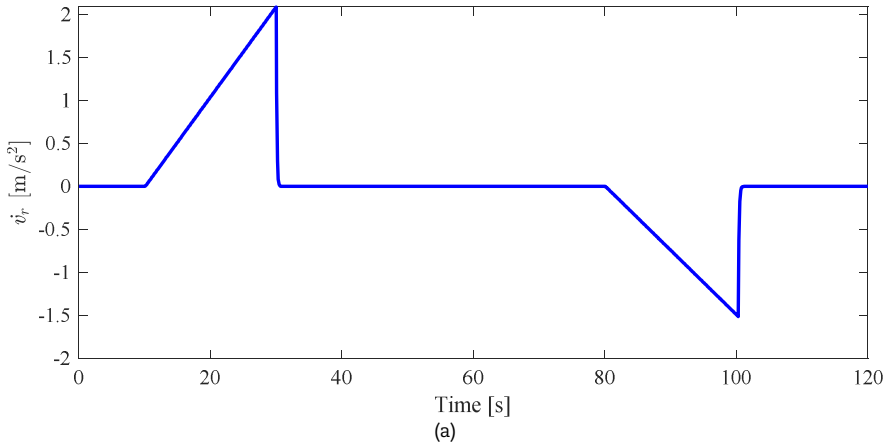


(a)

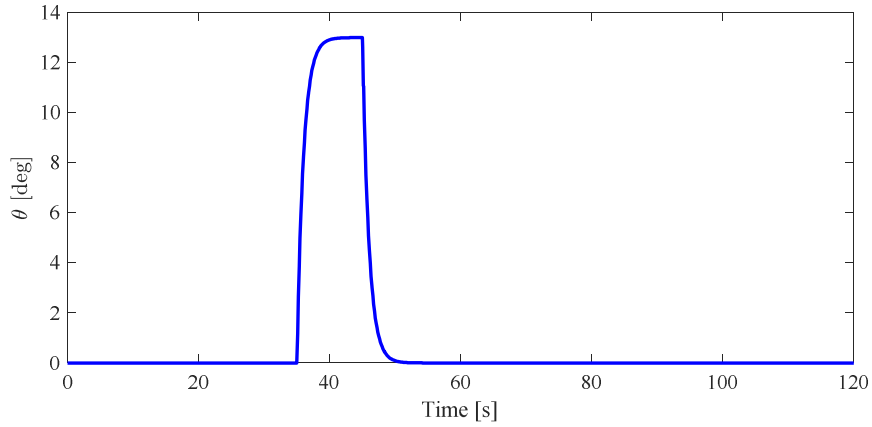


(b)

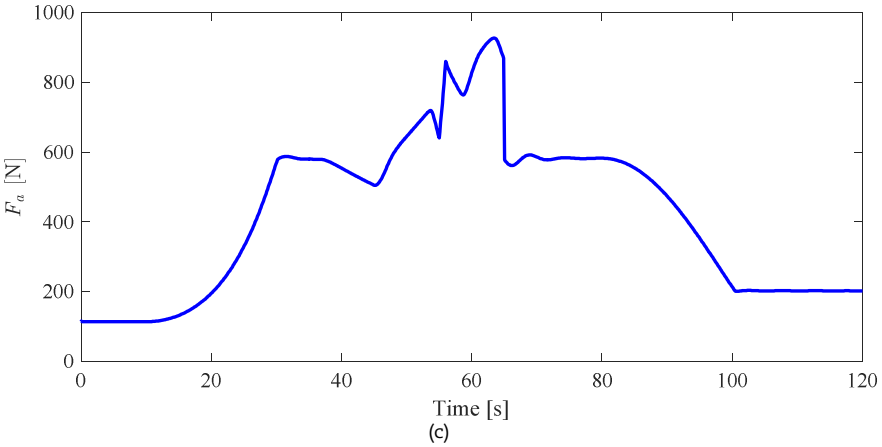


(c)

**Fig. 11.** Position control: (a) Acceleration, (b) Road slope, (c) Aerodynamic force disturbance.

From a vehicle stability standpoint, exceeding the permissible tire slip limit can lead to instability. Tire slip is directly related to the friction coefficient; therefore, a maximum allowable friction coefficient of 0.45 was incorporated into the controller design. A detailed analysis of Fig. 10(c) demonstrates that, under FCTS control, the tire saturation limit is maintained within acceptable bounds, with the friction coefficient remaining below the threshold of 0.45. This behavior is further confirmed in Fig. 10(b), which depicts the longitudinal tire force.

An analysis of Fig. 9(b) indicates that the speed tracking error of the FCTS algorithm reaches 17 km/h between 20 and 30 seconds, representing a notably high value. This occurrence is associated with reaching the tire saturation limit (Fig. 10(c)). Specifically, during the 20 to 30 second interval, the required longitudinal force to follow the reference speed signal exceeds the tire's frictional capacity. As a result, the controller cannot precisely track the reference speed, leading to an increased tracking error.

### 4.2. Longitudinal position control

The specifications of the designed scenario for evaluating position control are illustrated in Fig. 11. Careful examination of Fig. 11(a) shows that the acceleration increases linearly from zero to 2 m/s$^2$ between 10 and 30 seconds, and from zero to -1.5 m/s$^2$ between 80 and 100 seconds. The remainder of the maneuver is conducted at a constant speed. Furthermore, according to Fig. 11(b), the road slope is 13 deg between 35 and 45 seconds, while it remains zero for the rest of the maneuver. To account for disturbance effects, it is assumed that the longitudinal wind speed is 30 km/h between 55 and 65 seconds. This disturbance causes a sudden 30% increase in aerodynamic force (Fig. 11(c)). The total duration of the maneuver is considered to be 120 seconds.

The reference position signal, actual vehicle position, and tracking error associated with the proposed position control algorithm are displayed in Fig. 12. As shown in Fig. 12(a), both controllers initially demonstrate effective tracking of the reference position. However, due to the relatively large magnitude of the position values, the differences between the two controllers are not distinguishable in this figure. Consequently, the position tracking errors for both controllers are further illustrated in Fig. 12(b) to facilitate a more precise comparison. Analysis of the tracking error curves indicates that the maximum position tracking error for the FC controller is approximately 30 m, whereas, for the FCTS controller, it is around 15 m. Between 35 and 45 seconds, the tracking error of the FCTS algorithm increases to approximately 15 m. This increase is primarily due to the road slope during that interval, which requires a longitudinal force beyond the available tire-road friction capacity. Consequently, the vehicle cannot follow the reference trajectory with high precision during this period. As a result, the vehicle cannot precisely follow the reference trajectory.

A closer inspection of Fig. 9(b) reveals that the FC controller exhibits severe oscillations in the position tracking error, suggesting that the vehicle approaches instability. In contrast, under FCTS control, the vehicle response remains smooth and stable, with no significant oscillations. Moreover, regarding disturbance rejection, particularly during the 55 to 65-second interval, the proposed controller demonstrates superior performance compared to the FC controller.

A detailed analysis of Fig. 12(b) indicates that the FC controller displays significant oscillations in the position tracking error, suggesting potential stability concerns. Conversely, under FCTS control, the vehicle's response remains smooth and stable, with no notable oscillations observed. Additionally, regarding disturbance rejection, particularly within the 55 to 65-second interval, the proposed controller outperforms the FC controller, demonstrating improved robustness and effectiveness.

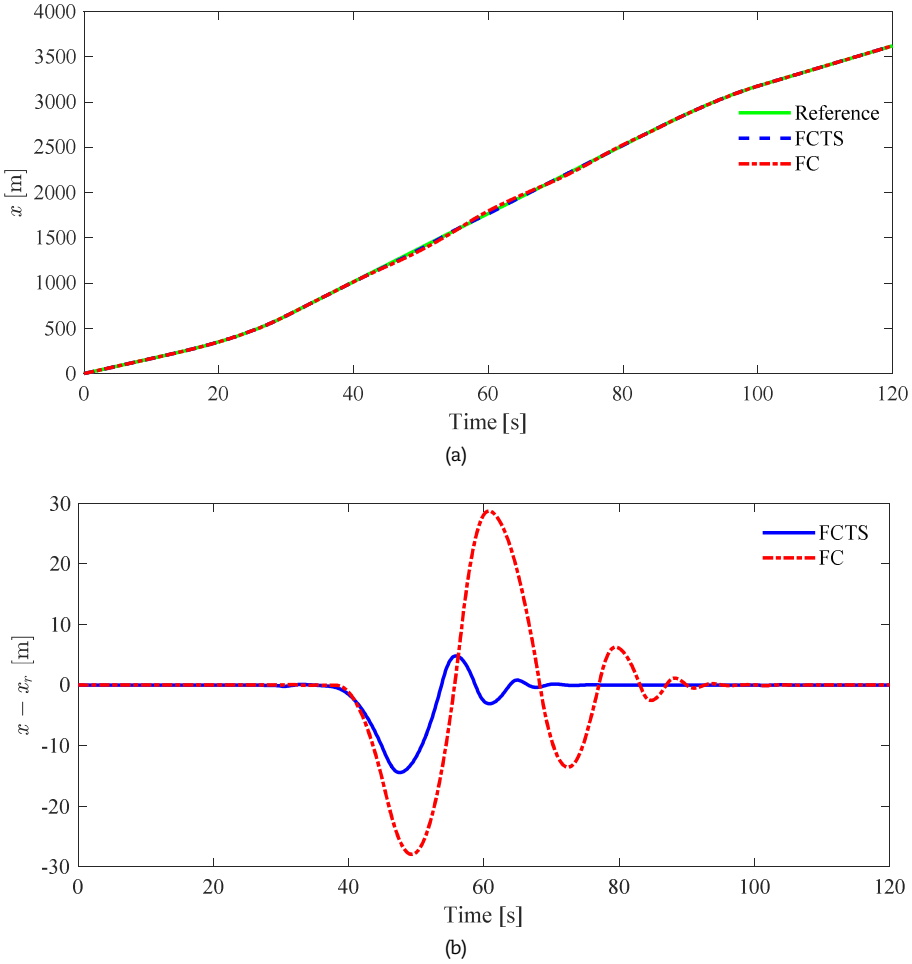


**Fig. 12.** Reference position tracking, (a) Speed, (b) Speed tracking error.

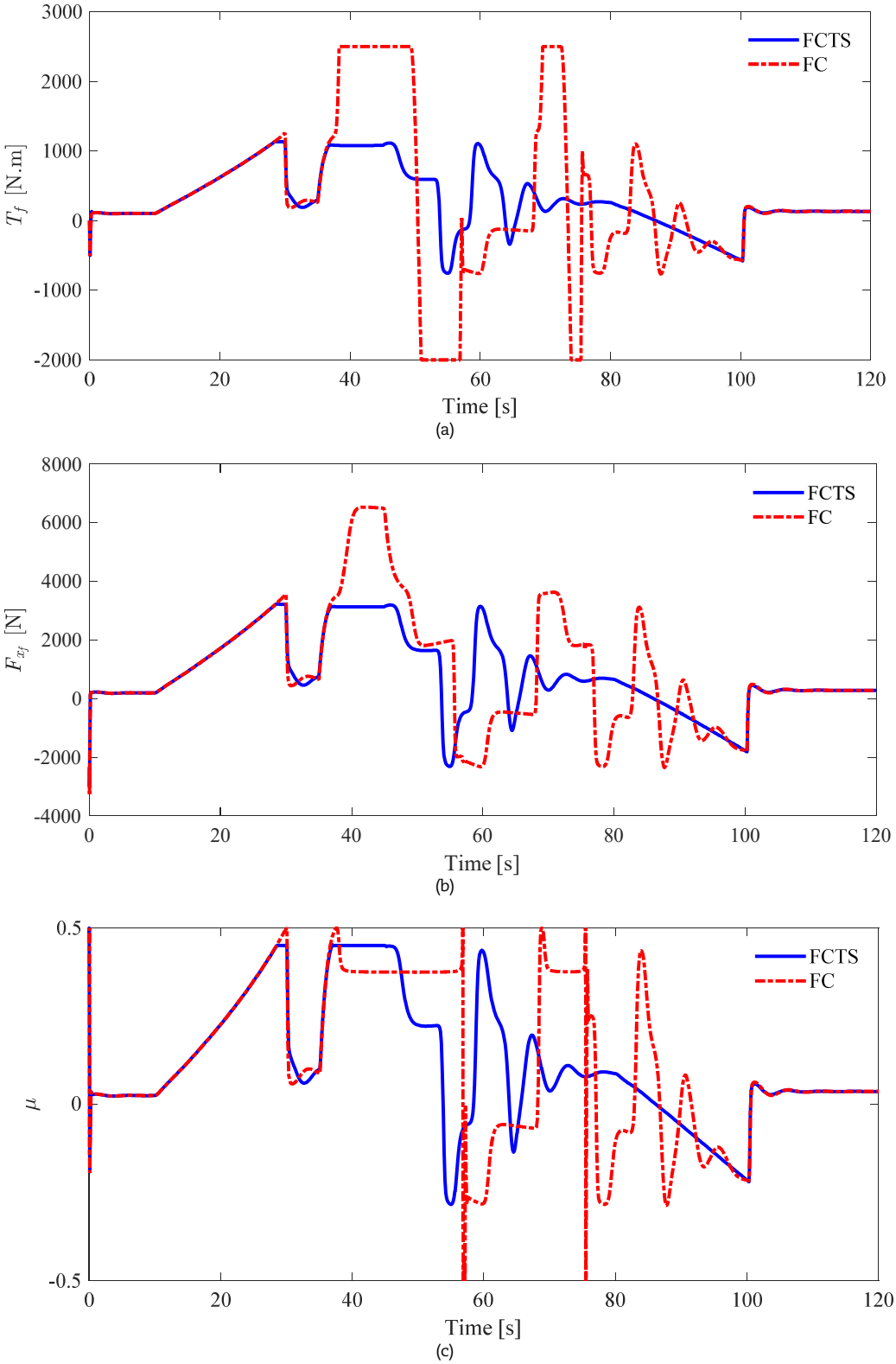


**Fig. 13.** Reference position control inputs, (a) Torque, (b) Longitudinal tire force, (c) Tire-road friction coefficient.

Concerning the stability and robustness of the FCTS controller, the results demonstrate that, within the time interval from 55 to 65 seconds, despite the disturbance caused by aerodynamic forces, the proposed control algorithm sustained satisfactory performance and accurately tracked the desired path.

To assess the control signals, the profiles of torque, longitudinal force, and tire-road friction coefficient are shown in Fig. 13. As illustrated in Fig. 13(a), the torque produced by the FC controller exhibits considerable oscillations and reaches the maximum permissible limit. In contrast, the torque under the FCTS control algorithm remains relatively steady and stays within acceptable bounds. As anticipated, the trends of the longitudinal force (Fig. 13(b)) and tire-road friction coefficient (Fig. 13(c)) closely mirror the torque behavior. Similarly, to the speed control scenario, the proposed position control strategy maintains the friction coefficient within the specified limit throughout the maneuver.

**Table 2.** Performance comparison of FCTS control versus FC (Speed control).

| Symbol | Evaluation index | Feedback control with tire saturation (FCTS) | Feedback control (FC) |
|---|---|---|---|
| Tracking Errors Index | $\int_0^{120} \lvert e_v \rvert \, dt$ | 69.64 | 220 |
| Control Inputs Index | $\int_0^{120} \lvert T_f \rvert \, dt$ | 42.36 | 76.31 |
| Power Consumption Index | $\int_0^{120} \lvert T_f . \omega \rvert \, dt$ | 1.41 | 27.17 |

**Table 3.** Performance comparison of FCTS control versus FC (Position control).

| Symbol | Evaluation index | Feedback control with tire saturation (FCTS) | Feedback control (FC) |
|---|---|---|---|
| Tracking Errors Index | $\int_0^{120} \lvert e_v \rvert \, dt$ | 149.06 | 604.4 |
| Control Inputs Index | $\int_0^{120} \lvert T_f \rvert \, dt$ | 49.54 | 92.18 |
| Power Consumption Index | $\int_0^{120} \lvert T_f . \omega \rvert \, dt$ | 1.37 | 39.11 |

### 4.3. Results Discussion

This section presents a numerical analysis comparing Feedback Control with tire Saturation (FCTS)and Feedback Control (FC) regarding both speed and position control performance.

**Speed Control.** A summary of the comparison results between the proposed FCTS control and FC control is provided in Table 2. The analysis of the error signals indicates that the integral of the FCTS velocity control error is approximately one-third of that observed in the FC control. Regarding the control inputs, the integral of the absolute control effort in FCTS is roughly 80% lower than that of FC. Additionally, the integral of the absolute power consumption in FC is about 19 times higher than that of FCTS. In conclusion, the proposed FCTS control demonstrates a significant advantage over the FC control in terms of both reference tracking accuracy and power efficiency.

**Position Control.** Table 3 summarizes the comparative performance of the proposed FCTS controller and the conventional FC scheme. Examination of the error profiles shows that the accumulated position error in FCTS is nearly one-fourth of that obtained using FC. With respect to the control input, the total absolute control effort required by the FC method is approximately 86 % greater than that of FCTS. Furthermore, the integrated absolute power consumption in FC exceeds that of FCTS by almost 26 times. These observations confirm the superior tracking precision and energy efficiency of the proposed FCTS control strategy.

In the proposed approach, distinct from traditional methods, the tire friction capacity—represented by the tire force saturation limit—is explicitly integrated into the controller design framework. By accounting for this nonlinear constraint, the controller effectively manages the driving torque applied to the wheels, ensuring it remains within physically permissible limits. This approach offers several key benefits. First, it prevents the tire from surpassing the allowable longitudinal slip ratio, thereby maintaining stable longitudinal vehicle dynamics and enhancing tracking accuracy. Second, it avoids the application of excessive or unnecessary torque, which reduces energy consumption and contributes to improved energy efficiency and extended vehicle range.

## 5. Conclusion

This study presented the design and evaluation of a robust control algorithm for managing the longitudinal dynamics of electric vehicles (EVs) under one-pedal driving conditions. The proposed controller explicitly incorporates tire force saturation into the control design, ensuring that control actions remain within the physical limits of the tire–road interaction. The algorithm combines both speed and position control elements, derived using Lyapunov stability theory, to guarantee asymptotic stability and reliable tracking performance. Comprehensive results were conducted under various challenging conditions, including road gradients, sudden aerodynamic disturbances, and nonlinear tire behavior. The results demonstrated that the proposed controller significantly enhances path-tracking accuracy and vehicle stability compared with conventional feedback control methods. Furthermore, the algorithm achieves smoother torque delivery, leading to reduced powertrain wear and improved passenger comfort. Quantitative comparisons confirmed a notable reduction in energy consumption, highlighting the efficiency benefits of the proposed approach. The incorporation of tire saturation constraints not only enhances safety under critical driving scenarios but also contributes to extending component lifespan and improving overall vehicle reliability. These findings suggest that the proposed control strategy is both practical and effective for real-world EV applications, particularly in systems implementing one-pedal driving functionality. For future research, the authors intend to extend this framework by incorporating lateral dynamics to achieve full vehicle motion control, integrating the proposed approach with adaptive estimation algorithms for real-time road friction identification. Further exploration into energy optimization and multi-objective control strategies is also envisioned to enhance system performance under diverse operating conditions.

## Author Contributions

The authors, H. Sazgar and A. Keymasi-Khalaji, contributed equally to this work.

## Acknowledgments

Not applicable.

## Conflict of Interest

The authors declared no competing interests for this paper.

## Funding

The authors claimed that there are no funds, grants, or other support devoted to the preparation of this manuscript.

## Data Availability Statements

The datasets used and/or analyzed during the current study are available from the corresponding author on reasonable request.

## Nomenclature

| | | | |
|---|---|---|---|
| $A_F$ | Effective frontal area of the vehicle [m²] | $T_{fr}$ | Reference torque [N/m] |
| $B, C, D$ | Tire model coefficients | $v$ | Vehicle's longitudinal speed [m/s] |
| $C_d$ | Aerodynamic drag coefficient | $V$ | Lyapunov candidate function |
| $F_{xf} / F_{xr}$ | Total longitudinal force of the front/rear axle tires [N] | $v_r$ | Reference vehicle speed [m/s] |
| $f_{roll}$ | Rolling resistance coefficient of the tire | $v_{rw}$ | Velocity of the wheel's contact point with the road surface [m/s] |
| $F_{zf} / F_{zr}$ | Vertical load on the front/rear axle [N] | $v_{wind}$ | Wind speed [m/s] |
| $g$ | Gravitational acceleration [m/s²] | $x$ | Vehicle position [m] |
| $h_a$ | Height of the location at which the equivalent aerodynamic force acts [m] | $x_r$ | Reference vehicle position [m] |
| $h_{CG}$ | CG height [m] | $\mu$ | Coefficient of friction between the tire and the road |
| $J_w$ | Rotational inertia of the wheel [kg/m²] | $\rho$ | Air density [kg/m³] |
| $K, K_1, K_2$ | Control gain | $\sigma$ | Longitudinal slip of the tire |
| $l_f / l_r$ | Distance between the front/ rear axles to CG [m] | $\omega_f / \omega_r$ | Angular velocity of the front/rear axle wheels [rad/s] |
| $m$ | Vehicle mass [kg] | $\omega_n$ | Natural frequency [rad/s] |
| $r_w$ | Effective wheel radius [m] | $\xi$ | Damping ratio |
| $T_f$ | Driving torque of the front axle [N/m] | $\theta$ | Road slope [rad] |

## References


[1] Emadi, A., *Handbook of Automotive Power Electronics and Motor Drives*, CRC Press, Boca Raton, 2005.
[2] Tanik, E., Parlaktas, V., Design of a very light L7e electric vehicle prototype, *International Journal of Automotive Technology*, 16(6), 2015,997-1005.
[3] Schafer, D., Lamantia, M., Chen, P., Modeling and spacing control for an electric vehicle with one-pedal-driving feature, *2021 IEEE American Control Conference (ACC)*, 2021.
[4] Nissan Motor, C., One-pedal driving explained, *Nissan Technical Report*, 2018.
[5] Singh, K. B., Taheri, S., Estimation of tire–road friction coefficient and its application in chassis control systems, *Systems Science & Control Engineering*, 3(1), 2015, 39-61.
[6] Pacejka, H. B., *Tire and Vehicle Dynamics*, 3rd ed, Butterworth-Heinemann, Oxford, 2012.
[7] Gillespie, T. D., *Fundamentals of Vehicle Dynamics*, SAE International, Warrendale, 1992.
[8] Chakraborty, S., Debraj, B., Protik, B., Dan, P., A systematic review on speed control modelling for electric vehicle, *Journal of Control and Decision*, 12(2), 2025, 167-94.
[9] Chu, L., Li, H., Xu, Y., Zhao, D., Sun, C., Research on longitudinal control algorithm of adaptive cruise control system for pure electric vehicles, *World Electric Vehicle Journal*, 14(2), 2023, 32.
[10] Shi, Q., He, Z., Wei, Y., Wang, M., Zheng, X., He, L., Single pedal control of battery electric vehicle by pedal torque demand with dynamic zero position, *IEEE Transactions on Intelligent Transportation Systems*, 23(11), 2022, 21608-19.
[11] Jalali, M., Hashemi, E., Khajepour, A., Chen, S.-K., Litkouhi, B., Integrated model predictive control and velocity estimation of electric vehicles, *Mechatronics*, 46, 2017, 84-100.
[12] Hua, L., Zhu, G., Closed-Loop Transient Longitudinal Trajectory Tracking for Connected Vehicles, *Machines*, 13(2), 2025, 163.
[13] Gao, H., Yang, H., Zhang, X., Ren, X., Liang, F., Yan, R., et al., Longitudinal velocity control of autonomous driving based on extended state observer, *CAAI Transactions on Intelligence Technology*, 10(1), 2025, 36-46.
[14] Qin, Z., Jing, H., Chen, L., Hu, M., Bian, Y., Cui, Q., Longitudinal vehicle stability control based on modified sliding mode control, *Automotive Innovation*, 7(2), 2024, 335-48.
[15] Alika, R., Mellouli, E. M., Tissir, E. H., A modified sliding mode controller based on fuzzy logic to control the longitudinal dynamics of the autonomous vehicle, *Results in Engineering*, 22, 2024, 102120.
[16] Islam, F., Ball, J. E., Goodin, C. T., Enhancing longitudinal velocity control with attention mechanism-based deep deterministic policy gradient (DDPG) for safety and comfort, *IEEE Access*,12, 2024, 30765-80.
[17] Alika, R., Mellouli, E. M., Tissir, E. H., Adaptive cruise control of the autonomous vehicle based on sliding mode controller using arduino and ultrasonic sensor, *Journal of Robotics and Control (JRC)*, 5(1), 2024, 301-11.
[18] Jo, A., Lee, H., Seo, D., Yi, K., Model-reference adaptive sliding mode control of longitudinal speed tracking for autonomous vehicles, *Proceedings of the Institution of Mechanical Engineers, Part D: Journal of Automobile Engineering*, 237(2-3), 2023, 493-515.
[19] Wang, Y., Deng, Y., Wang, H., Zuo, Z., Model predictive control-based longitudinal control for autonomous electric vehicle with changing mass, *Asian Journal of Control*, 25(2), 2023, 1297-309.
[20] Wang, H., Zuo, Z., Wang, Y., Yang, H., Hu, C., Longitudinal velocity regulation of UGVs: A composite control approach for acceleration and deceleration, *IEEE Transactions on Intelligent Transportation Systems*, 24(10), 2023, 11096-106.
[21] Fei, H., Xin, G., Hao, J., Chunguang, D., Intelligent vehicle longitudinal acceleration control method based on feedforward and feedback combination, *Proceedings of the Institution of Mechanical Engineers, Part D: Journal of Automobile Engineering*, 237(5), 2023, 1065-81.
[22] Oudjama, F., Boumediene, A., Saidi, K., Boubekeur, D., Robust speed control in nonlinear electric vehicles using H-infinity control and the LMI approach, *Journal of Intelligent Systems and Control*, 2(3), 2023, 170-82.
[23] Berntorp, K., Quirynen, R., Uno, T., Di Cairano, S., Trajectory tracking for autonomous vehicles on varying road surfaces by friction-adaptive nonlinear model predictive control, *Vehicle System Dynamics*, 58(5), 2020, 705-25.
[24] Hu, J., Rakheja, S., Zhang, Y., Real-time estimation of tire–road friction coefficient based on lateral vehicle dynamics, *Proceedings of the Institution of Mechanical Engineers, Part D: Journal of Automobile Engineering*, 234(10-11), 2020, 2444-57.
[25] Zhao, Y., Lin, F., *Vehicle Stability Control and Estimation of Road Friction Coefficient Based on Vehicle Longitudinal Dynamics*, Springer, Singapore, 2024.
[26] Pappalardo, C. M., Lombardi, N., Guida, D., A model-based system engineering approach for the virtual prototyping of an electric vehicle of class l7, *Engineering Letters*, 28(1), 2020, 215-34.
[27] Bakker, E., Nyborg, L., Pacejka, H. B., Tyre modelling for use in vehicle dynamics studies, *SAE Transactions*, 1987, 190-204.


## ORCID iD


Hadi Sazgar https://orcid.org/0000-0002-2208-727X
Ali Keymasi-Khalaji https://orcid.org/0000-0001-5414-6046



© 2025 Shahid Chamran University of Ahvaz, Ahvaz, Iran. This article is an open access article distributed under the terms and conditions of the Creative Commons Attribution-NonCommercial 4.0 International (CC BY-NC 4.0 license) (http://creativecommons.org/licenses/by-nc/4.0/).

**How to cite this article:** Sazgar H., Keymasi-Khalaji A. Longitudinal Control of Electric Vehicles under One-Pedal Driving Conditions Considering Tire–Road Friction Capacity, *J. Appl. Comput. Mech.*, 12(4), 2026, 1411-1426. https://doi.org/10.22055/jacm.2025.48708.5441

**Publisher's Note** Shahid Chamran University of Ahvaz remains neutral with regard to jurisdictional claims in published maps and institutional affiliations.